




Different spin relaxation properties observed in linearly and circularly polarized laser induced terahertz emission from a Bi/Co bilayer

Kazuaki Ishibashi ^{1,2,*}, Satoshi Iihama ^{3,2,†} and Shigemi Mizukami ^{2,4}

¹*Department of Applied Physics, Graduate School of Engineering, Tohoku University, Sendai 980-8579, Japan*

²*WPI Advanced Institute for Materials Research, Tohoku University, 2-1-1, Katahira, Sendai 980-8577, Japan*

³*Frontier Research Institute for Interdisciplinary Sciences, Tohoku University, Sendai 980-8578, Japan*

⁴*Center for Science and Innovation in Spintronics, Core Research Cluster, Tohoku University, Sendai 980-8577, Japan*



(Received 26 December 2022; revised 27 February 2023; accepted 29 March 2023; published 10 April 2023)

Recently, a helicity-dependent photocurrent was reported in Bi single-layer thin films. It is proposed that the origin of this photocurrent is the combination of photon-spin conversion and spin-charge conversion effects in Bi, and efficient spin conversion in Bi is expected. In this study, we measure two types of terahertz (THz) emissions from Bi/Co bilayer films induced by spin current generation using laser induced demagnetization of the Co layer and the photon-spin conversion effect in the Bi layer to investigate the spin current induced by the two mechanisms simultaneously. We clearly observe different Bi thickness dependences of peak intensity and bandwidth for THz spin current in two experiments, i.e., spin current induced by demagnetization of Co and by photon-spin conversion in Bi. The different Bi thickness dependences of spin current intensity and bandwidth in two experiments are caused by different spin relaxation properties of optically excited spin currents in Bi layers.

DOI: [10.1103/PhysRevB.107.144413](https://doi.org/10.1103/PhysRevB.107.144413)

I. INTRODUCTION

Conversion between electron spin and physical quantities, such as charge, light, heat, and phonons, is one of the fundamental principles that enable the generation and detection of the spin current [1–4]. To enhance the conversion efficiency of future spintronic devices, numerous studies have explored various materials, such as topological materials [5,6] and heavy metals (e.g., Pt, W, Ta, and Bi [7–12]). In particular, Bi is the basis of several topological materials, such as $\text{Bi}_{0.9}\text{Sb}_{0.1}$, PtBi_2 , and $\text{Bi}_x\text{Se}_{1-x}$ [13–15]. Accordingly, Bi-based alloys are among the candidate materials with good spin current generation characteristics owing to their large spin-orbit coupling and unique band structure. Thus, it is important to investigate the phenomena occurring in Bi to obtain a basic understanding of the phenomena occurring in Bi-based alloys. In addition, Bi itself is expected to exhibit an efficient spin conversion effect and other interesting phenomena [16].

Recently, a helicity-dependent (HD) photocurrent in Bi single-layer thin films and Bi/Cu(or Ag) bilayer films was observed via pulse laser induced terahertz (THz) emission [17] and transport measurement using a continuous-wave laser [18]. The proposed mechanism for photocurrent in Bi is the photoinduced inverse spin-Hall effect [19]. A circularly polarized laser induces electron spin in Bi depending on the optical helicity via conversion from photon spin angular momentum (SAM) to electron SAM, which is called the photon-spin conversion effect. Subsequently, the flow of electron SAM

is converted to charge current through the inverse spin-Hall effect. Although photon SAM driven torques were observed in heavy metal/ferromagnet bilayer films via measurement of the time-resolved magneto-optical Kerr effect [2,20–22], the above-mentioned HD photocurrent in a single-layer thin film has been mostly reported in Bi-related materials [17,18,23]. Therefore, the efficient photon-spin conversion effect in Bi is expected, which most likely originates from the band structure inherent in semimetallic Bi. However, the details of photon-spin conversion in Bi have not been clarified yet because the photon-spin conversion and spin-charge conversion effects are observed simultaneously in the photocurrent measurement; thus, one cannot distinguish between two spin-related conversion effects.

In this study, to disentangle the two processes, namely, the photon-spin conversion and spin-charge conversion effects, and gain insight into the underlying physics, we measure the THz emission induced by spin current generation using photon-spin conversion and laser induced demagnetization simultaneously in Bi/Co bilayer films.

THz emission experiments conducted with structures widely used in spintronics THz emitters [24–26], e.g., ferromagnet/Bi bilayers, remain scarce. When a femtosecond laser pulse is irradiated on the ferromagnet/Bi bilayer, spin current can be generated by the ultrafast demagnetization of the ferromagnetic layer due to the conservation of angular momentum [27–29]. This transient spin current is converted into charge current owing to spin-charge conversion effect in the Bi layer, and then a THz wave is emitted. Thus, we can simultaneously investigate the difference in the spin current via photon-spin conversion and laser induced demagnetization using this structure.

*kazuaki.ishibashi.p1@dc.tohoku.ac.jp

†satoshi.iihama.d6@tohoku.ac.jp

II. EXPERIMENT

The samples were prepared using DC/RF magnetron sputtering. The stacking structure of samples was glass substrate/Bi(d_{Bi})/Co(5)/MgO(2)/Ta(2) (thickness is in nanometers). The thicknesses of the Bi layers d_{Bi} were varied from 10 to 120 nm. The Co layer generates the spin current from laser induced demagnetization. The Bi layers generate spin current via the photon-spin conversion effect and convert the spin current into charge current via the spin-charge conversion effect. The MgO and Ta layers are capping layers to prevent oxidization. The Bi film in all samples was polycrystalline, with the (003) and (012) preferred orientations indexed using hexagonal notation. The saturation magnetization of Co was almost constant with respect to Bi thickness (see Appendix A for details on sample information).

The laser pulse induced THz emission from Bi/Co films was measured using THz time domain spectroscopy [30–32]. Laser pulses are generated by a Ti:sapphire femtosecond laser with a wavelength of 800 nm, pulse duration of 160 fs, and repetition rate of 1 kHz. Pump laser pulses are modulated by a mechanical chopper at a frequency of 360 Hz. A quarter-wave plate is placed in front of the samples to control pump laser polarization. The pump laser was focused on the film with a fluence of 0.62 mJ/cm². The polarization of the THz wave emitted from the sample surface was analyzed with two wire grids [33,34]. We measured the emitted THz wave using the electro-optic (EO) sampling method [35] with a 1-mm-thick ZnTe(110) crystal. All measurements were taken at room temperature.

III. EXPERIMENTAL RESULTS AND DISCUSSION

A. Laser induced THz emission and Bi thickness dependence

We measured two kinds of THz waves emitted from Bi/Co bilayer films induced by linearly polarized and circularly polarized lasers, as shown in Figs. 1(a) and 1(b), respectively. The difference between the two measurements is the source of spin current. The first spin current source is laser induced demagnetization. When a linearly polarized laser is irradiated on the sample, ultrafast spin current is generated from the laser induced demagnetization of Co, where the polarization of spin is parallel to the magnetization direction of Co. This spin current flows into an adjacent Bi layer and

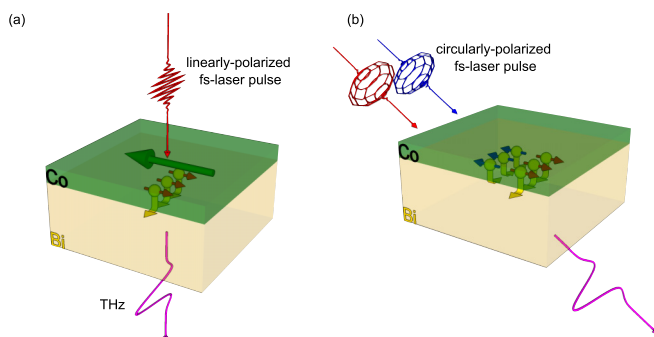


FIG. 1. Schematic illustration of (a) linearly and (b) circularly polarized laser induced terahertz emission from a Bi/Co bilayer.

is converted to charge current through the inverse spin-Hall effect in Bi, which causes THz emission from the film surface [Fig. 1(a)]. The second source is photon-spin injection via the photon-spin conversion effect in Bi. When a circularly polarized laser is irradiated on the sample with an oblique incidence, in-plane electron spin is injected in Bi depending on the optical helicity via the photon-spin conversion effect. The incident angle was fixed at 45° in our measurement. Spin current is caused by the gradient of induced spin because of the finite penetration depth of the laser. This spin current is converted into a charge current, and then the THz wave is emitted [Fig. 1(b)]. In contrast to the linearly polarized laser induced THz emission, circularly polarized laser induced THz emission is observed in Bi single-layer thin films [17]. We conducted THz experiments using spin currents generated by two different mechanisms, as shown in Figs. 1(a) and 1(b), where the THz wave polarization induced by demagnetization is orthogonal to that induced by photon-spin injection to distinguish the two contributions via THz polarization analysis with two wire grids. Note that we measured photon-spin conversion induced terahertz emission with no net magnetization of Co; that is, samples in a virgin state were measured for THz emission induced by photon-spin conversion in Bi. This no net magnetization was confirmed by measuring the orthogonal component of the THz signal. The HD-THz signal caused by the inverse Faraday effect and the inverse spin-orbit torque observed in a previous study [36] can be ruled out because of the lack of net magnetization of Co.

A typical THz signal V_{THz} induced by a linearly polarized laser with two opposite sample magnetization $\pm M$ orientations is shown in Fig. 2(a). The THz signal is inverted when the magnetization is reversed, which is consistent with THz signals emitted from magnetic heterostructures [24,26]. It was found that there is a contribution from the ordinary Nernst effect in Bi [37] where the THz signal is linearly changed based on the external magnetic field strength. To remove the contribution of the ordinary Nernst effect, first, an external magnetic field was applied to saturate the magnetization of Co, and then the THz signal was measured without an external magnetic field. Figure 2(b) shows typical circularly polarized laser pulse induced THz signals V_{THz} with different optical helicities σ_{\pm} . The red and blue circles represent the THz signals induced by right- and left-circularly polarized lasers, respectively. The sign of the THz signal is reversed when the helicity of the circularly polarized laser pulse is changed, indicating the HD-THz signal. To focus on the HD and magnetization direction dependent contributions, we considered antisymmetric signals with respect to magnetization and optical helicity, i.e., $[V_{\text{THz}}(+M) - V_{\text{THz}}(-M)]/2$ and $[V_{\text{THz}}(\sigma+) - V_{\text{THz}}(\sigma-)]/2$.

Figures 2(c) and 2(d) show the Bi thickness d_{Bi} dependence of the linearly polarized laser induced THz signal and HD circularly polarized laser induced THz signal, respectively. As the Bi thickness d_{Bi} increases from 20 to 120 nm, the amplitude of the THz signal induced by the linearly polarized laser decreases. In contrast to the linearly polarized laser induced THz signal, the amplitude of the HD-THz signal induced by the circularly polarized laser increases. Figures 3(a) and 3(b) exhibit the d_{Bi} dependence of the peak value of the linearly polarized laser induced THz signal and HD circularly polarized laser induced THz signal, respectively. Different d_{Bi}

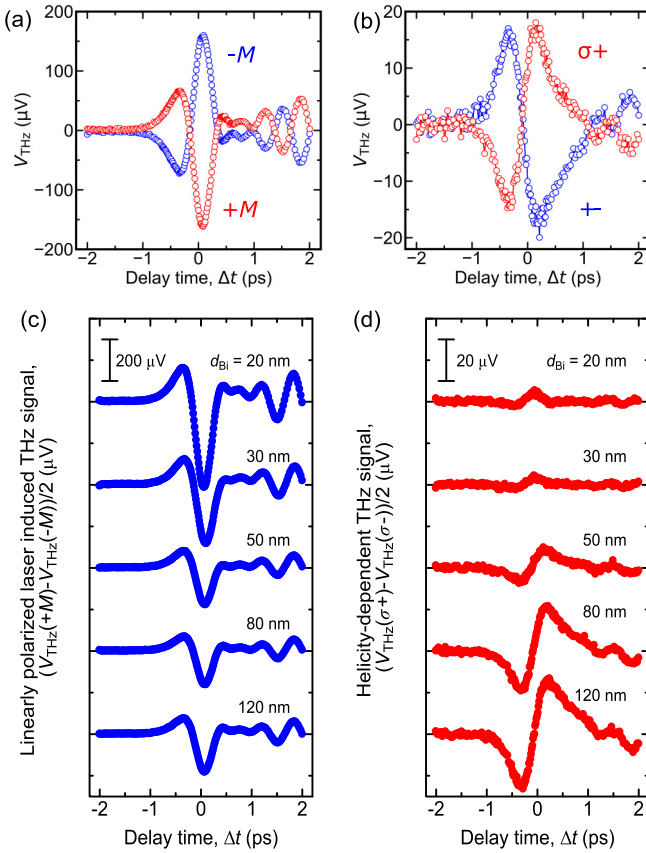


FIG. 2. (a) Linearly polarized laser induced terahertz signal with different polarities of Co magnetization, where the laser is irradiated with normal incidence. (b) Circularly polarized laser induced terahertz signal with different helicities of the laser pulse, where the laser is irradiated with a 45° incident angle. Bi thickness d_{Bi} dependence of (c) the linearly polarized laser induced terahertz signal and (d) the HD circularly polarized laser induced terahertz signal, where the difference between signals obtained with left- and right-circularly polarized light is taken.

dependences are clearly observed in the two experiments. The trends observed in the two experiments, shown in Figs. 3(a) and 3(b), are consistent with those observed in previous studies [17,26]. Moreover, the wave form of the THz signal was different; that is, the shape is broader for the HD-THz signal compared with the linearly polarized laser induced THz

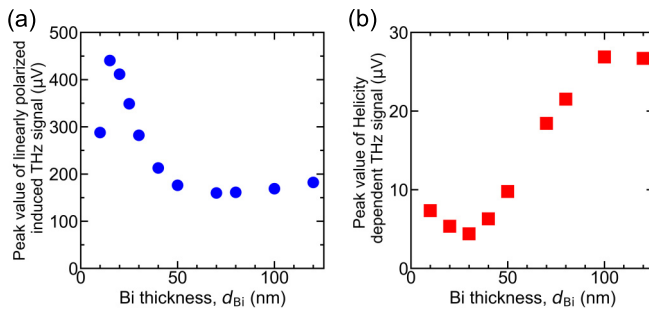


FIG. 3. Peak value of (a) linearly polarized laser induced terahertz signal and (b) HD terahertz signal plotted as a function of Bi thickness d_{Bi} .

signal. Those differences can be caused by different temporal dynamics of the laser induced spin current. To obtain the temporal spin current, we analyzed THz signals as described below.

B. Spin current analyzed from experiment

THz signals measured via the EO sampling method can be converted into THz electric field in the sample and temporal spin current. In the frequency domain, the relation between the measured THz signal V_{THz} and THz electric field E is stated as [25]

$$V_{\text{THz}}(\omega) \propto H(\omega)E(\omega), \quad (1)$$

where $H(\omega)$ is the response function of the THz detection process. The response function comprises the propagation of the THz pulse from the sample to the detector and the detector response function for the ZnTe(110) crystal. The detection of the THz electric field is assumed to be far field; that is, the response function for propagation is proportional to the frequency. The detector response function for the ZnTe crystal was calculated with parameters taken from Ref. [38]. The THz electric field generated from the laser induced spin current is described as [25]

$$E(\omega) = eZ(\omega)\theta_{\text{SH}} \int_0^{d_{\text{Bi}}} J_s(z, \omega) dz, \quad (2)$$

where θ_{SH} and e are the spin-Hall angle and electron charge, respectively. In addition, $J_s(\omega)$ represents spin current in the frequency domain. The electromagnetic impedance $Z(\omega)$ is expressed as

$$Z(\omega) = \frac{Z_0}{n_0 + n_{\text{sub}} + Z_0\sigma_{\text{tot}}(\omega)d_{\text{tot}}}, \quad (3)$$

where Z_0 , n_0 , n_{sub} , and d_{tot} are the vacuum impedance, refractive index of air, refractive index of the substrate, and total film thickness, respectively. Here, $n_0 = 1.0$, and $n_{\text{sub}} = 1.5$. $\sigma_{\text{tot}}(\omega)$ is the total conductivity, which was assumed to be constant in the THz range [17,39]. σ_{tot} values were measured using the four-point probe method (see Appendix B for the electrical conductivity of samples).

Using Eqs. (1)–(3) and the measured THz signals, the spin current was obtained with a cutoff frequency of 3 THz. Figures 4(a) and 4(b) show the temporal spin current $\int_0^{d_{\text{Bi}}} J_s(z, t) dz$ obtained from the linearly and circularly polarized laser induced THz signals for the Bi(80)/Co(5) bilayer film, respectively. Figures 4(c) and 4(d) show the Fourier transformation spectrum $\int_0^{d_{\text{Bi}}} J_s(z, \omega) dz$ for the spin currents depicted in Figs. 4(a) and 4(b), respectively. The solid curve denotes the result fitted with the Lorentzian; subsequently, the bandwidth Δf of the spectrum for the spin current is evaluated. The peak values of the spin current and bandwidth Δf plotted as a function of Bi thickness d_{Bi} are shown in Figs. 4(e) and 4(f), respectively. Blue solid symbols and red open symbols represent the values obtained from linearly and circularly polarized laser induced spin currents, respectively. The intensity of the spin current induced by the linearly polarized laser peaked at approximately $d_{\text{Bi}} = 20$ nm [solid circles in Fig. 4(e)], whereas the amplitude of the spin current

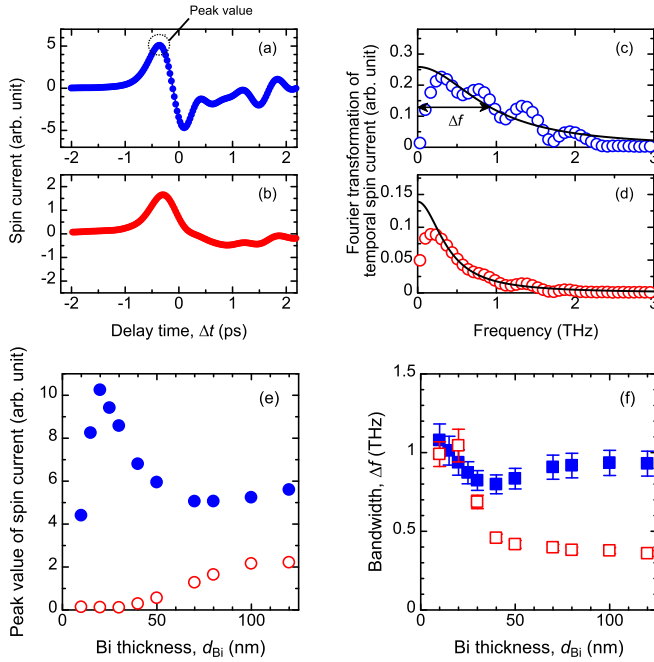


FIG. 4. Temporal spin current signal obtained from (a) the linearly polarized laser induced terahertz signal and (b) the circularly polarized laser induced terahertz signal for the Bi(80)/Co(5) bilayer. (c) Fourier transformation spectrum for spin current induced by (c) a linearly polarized laser and (d) a circularly polarized laser, corresponding to (a) and (b). Solid curves represent Lorentzian fitting to obtain the bandwidth of the spectra. (e) Peak value of spin current plotted as a function of Bi thickness d_{Bi} . (f) Bandwidth of the Fourier transformation spectrum Δf plotted as a function of d_{Bi} .

induced by the circularly polarized laser peaked at approximately $d_{\text{Bi}} = 100$ nm [open circles in Fig. 4(e)]. Δf of the spin current induced by the linearly polarized laser was almost constant with respect to Bi thickness d_{Bi} [solid squares in Fig. 4(f)]. On the other hand, Δf of the spin current induced by the circularly polarized laser exhibited a decreasing trend as d_{Bi} increased and then saturated to a constant [open squares in Fig. 4(f)]. In addition, Δf of the spin current induced by the circularly polarized laser was one half of that induced by the linearly polarized laser when Bi thickness is sufficiently thick. The differences can be caused by the difference in the source of the spin current and spin transport, as discussed in the next section.

C. Theoretical analysis of spin current

To explain the d_{Bi} dependence of the laser induced spin current, we performed a simulation of the spin-diffusion equation. Superdiffusive transport and Boltzmann transport approaches more rigorously depict interacting electron kinetics with various energy scales far from the thermal equilibrium state [40,41]. However, these models are quite complex since one needs to consider electron energy, momentum, and scattering properly. In the diffusive approach, the backflow spin current cannot be reproduced, and it is implicitly assumed that spin angular momentum moves based on the continuity equation and that there is electron scattering during spin transport. The spin transport in the spin-diffusion equation can be simply

described by how fast spin angular momentum is diffused and lost. The spin-diffusion equation is described as follows [42]:

$$\frac{\partial s(z, t)}{\partial t} = D \frac{\partial^2 s(z, t)}{\partial z^2} - \frac{s(z, t)}{\tau_s} + Q_s(z, t), \quad (4)$$

where s , D , and τ_s denote the electron SAM density, diffusion constant, and spin relaxation time, respectively. Here, Q_s corresponds to the source term for the spin current, and we assumed two different spin current sources in two experiments, as described below. First, demagnetization is considered a spin source at the interface between the Co and Bi layers Q_s^d , which can be expressed as follows:

$$Q_s^d(z, t) = \begin{cases} -\frac{d_{\text{Co}}}{\gamma} \frac{d}{dt} [\Delta M_s(t; d_{\text{Bi}})] & \text{if } z = d_{\text{Bi}}, \\ 0 & \text{else,} \end{cases} \quad (5)$$

where γ and ΔM_s denote the gyromagnetic ratio and temporal dynamics of demagnetization, respectively. ΔM_s was evaluated by using the time-resolved magneto-optical Kerr effect (TRMOKE) measurement [43] with a constant pump fluence of 0.62 mJ/cm^2 . The laser induced spin current was considered to be inversely proportional to the total layer thicknesses for spintronic THz emitters described in a previous study [25]. In fact, laser induced demagnetization decreased with increasing d_{Bi} values (see Appendix D for the d_{Bi} dependence of demagnetization), which is consistent with the assumption that the absorbed fluence per unit thickness decreases with an increase in the metallic layer thickness. Therefore, we considered the d_{Bi} dependence of demagnetization $\Delta M_s(t; d_{\text{Bi}})$, which is proportional to $(d_{\text{Bi}} + d_{\text{Co}})^{-1}$, i.e., $\Delta M_s(t; d_{\text{Bi}}) = \Delta M_s(t; d_{\text{Bi}} = 15)(15 + d_{\text{Co}})/(d_{\text{Bi}} + d_{\text{Co}})$, using the demagnetization dynamics for a 15-nm-thick Bi sample, $\Delta M_s(t; d_{\text{Bi}} = 15)$.

On the other hand, photon-spin injection is considered to be a spin current source for circularly polarized laser induced THz signals. photon-spin conversion induced spin density Q_s^p can be considered the conversion between absorbed photon SAM and electron SAM, which is described by the following equation [22]:

$$Q_s^p(z, t) = \frac{\eta a(z) F_p}{\omega_l} \sin \theta_{\text{inc}} G(t), \quad (6)$$

where F_p , ω_l , θ_{inc} , and $G(t)$ denote the fluence of the pump laser, laser angular frequency, the incident angle of laser, and the temporal profile of the Gaussian laser pulse, respectively. The laser absorption profile inside the Bi layer $a(z)$ is calculated using the transfer matrix method [44] (see Appendix C for refractive index and light absorption). Here, we assume that photon SAM is entirely converted into electron SAM, i.e., $\eta = 1$. The obtained $s(z, t)$ can be converted into spin current via the following relation:

$$J_s(z, t) = D \frac{\partial s(z, t)}{\partial z}. \quad (7)$$

Using Eqs. (4)–(7), simulations with various D and τ_s values were performed (see Appendix E for details of simulation results), and temporal spin current I_s integrated across the Bi layer, namely, $\int_0^{d_{\text{Bi}}} J_s(z, t) dz$, was obtained.

Figures 5(a) and 5(b) show the simulated temporal spin current induced by the demagnetization of the Co layer and

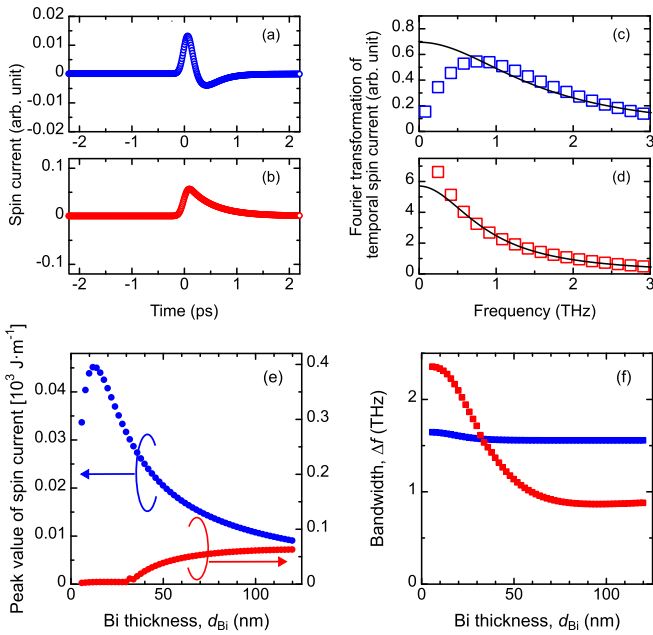


FIG. 5. Temporal spin current induced by (a) demagnetization of the Co layer and (b) photon-spin injection into the Bi layer, calculated by the spin-diffusion equation. (c) and (d) Fourier transformation spectrum for spin current corresponding to (a) and (b). (e) Peak values of spin current obtained with the spin-diffusion simulation plotted as a function of Bi thickness d_{Bi} . (f) Bandwidth of the Fourier transformation spectrum Δf obtained with the spin-diffusion simulation plotted as a function of d_{Bi} .

photon-spin injection into the Bi layer, respectively. Figures 5(c) and 5(d) show the Fourier transformation spectra for spin currents corresponding to Figs. 5(a) and 5(b), respectively. The solid curve represents the result fitted with the Lorentzian function to evaluate the bandwidth Δf . The obtained peak values and bandwidth of the spin current plotted as a function of Bi thickness are shown in Figs. 5(e) and 5(f). Simulation results roughly agree with experimentally observed Bi thickness dependence.

D. Discussion

The initial sharp increase in the demagnetization induced spin current is due to the spin diffusion in the Bi layer. The decrease of more than 20 nm was mainly caused by the decline in the spin current generated by the demagnetization of the Co layer as mentioned above [depicted by the solid blue symbols in Figs. 4(e) and 5(e)]. The photon-spin conversion induced spin current in the thin region is negligible, which is attributed to the small light absorption in the Bi layer (see Appendix C for the laser absorption profile). In the thick region, the peak value of the spin current induced by photon-spin conversion gradually increases, which corresponds to the spin diffusion in the Bi layer [open red circles in Fig. 4(e) and solid red circles in Fig. 5(e)]. Since the spin current reaches a maximum when d_{Bi} is around 80–100 nm, which is quite thick compared with the light penetration depth of Bi (~ 16 nm), the increasing trends in Figs. 4(e) and 5(e) are not due to light penetration effect. Similarly, Δf remains almost constant for the spin current induced by demagnetization and decreases with an

increase in d_{Bi} for the spin current induced by photon-spin injection, which is obtained in the simulation [Figs. 4(f) and 5(f)]. The parameters used in Figs. 5(e) and 5(f) are $D = 1.2 \times 10^{-3} \text{ m}^2/\text{s}$ and $\tau_s = 0.04 \text{ ps}$ for the demagnetization induced spin current and $D = 1.2 \times 10^{-3} \text{ m}^2/\text{s}$ and $\tau_s = 4 \text{ ps}$ for the photon-spin conversion induced spin current. D used in the simulation is obtained based on the electrical conductivity of the sample (see Appendix B) and the Wiedemann-Franz law. τ_s values were not evaluated by the fitting calculation but extracted by comparing the d_{Bi} dependences of spin current intensity and Δf obtained in the experiment and calculation with changing parameter values which have an order of magnitude different (see Appendix E). Extracted quantities such as τ_s are not rigorous and likely have an uncertainty due to limitations of modeling. The backflow spin current observed in the photon-spin conversion induced spin current [opposite polarity at around 1 ps in Fig. 4(b)] cannot be reproduced by the spin-diffusion modeling. Even with the above-mentioned uncertainty, the d_{Bi} dependence of the spin current intensity and bandwidth can be explained qualitatively by the spin-diffusion simulation, as shown in Figs. 5(e) and 5(f). Note that the τ_s values used in the two experiments to explain the experimental results are two orders of magnitude different from each other. It should also be mentioned that a possible explanation for the obvious change in the THz wave form from increasing Bi thickness in Fig. 2(d) is attributed to large τ_s of electron spins excited by photon-spin conversion in Bi. In fact, the increasing slope of the peak spin current value for demagnetization is much higher than that for photon-spin conversion, which is due to different spin relaxation lengths in the two experiments. This indicates that the spin relaxation length (here, we discuss $\sqrt{D\tau_s}$) for demagnetization induced spin current is one order of magnitude shorter than that for photon-spin injection induced spin current.

The differences in the spin relaxation property should be related to the energy level of the spin transport for optically excited electron spins. The electron spin characteristics at the Fermi level are different from those at the optically excited state. The mechanism behind the spin current generated by laser induced demagnetization is an s - d exchange coupling. The optically excited electron relaxes back to the Fermi-Dirac distribution after several tens to hundreds of femtoseconds [45]. Then, the loss of angular momentum in the local magnetic moment due to demagnetization transfers the angular momentum to mobile s electrons owing to the s - d exchange coupling [46]. Although a shorter spin relaxation length of the laser induced spin current in ferromagnet/nonmagnet heterostructures, which might be attributed to optically excited electrons, has been observed [47–49], the energy level of the electron spins may be close to the Fermi level. On the other hand, spin current generated by photon-spin conversion is possibly carried by optically excited electron spins in Bi. The recombination time of optically excited electrons with 800-nm wavelength light is $\sim 4 \text{ ps}$ [50], similar to the timescale of the spin relaxation time used in this study, indicating that spin relaxation is mediated by the recombination of optically excited electrons and holes. This fact indicates that the spin relaxation length of optically excited spins in Bi is likely longer than those near the Fermi level, which possibly stems from the semimetallic characteristics of Bi.

IV. CONCLUSION

In this study, two kinds of THz emissions from Bi/Co bilayer films induced by spin current generation due to demagnetization and the photon-spin conversion effect with various Bi thicknesses were investigated simultaneously. The spin current peak intensity and bandwidth were discussed based on the spin-diffusion simulation with different spin current sources, namely, the demagnetization of Co and photon-spin conversion in Bi. The experimental and simulation results revealed that the spin relaxation length of electron spins excited by the photon-spin conversion in Bi is much longer than that induced by the demagnetization of Co, which might be attributed to the semimetallic characteristics of Bi.

ACKNOWLEDGMENTS

This study is partially supported by KAKENHI (Grants No. 19K15430 and No. 21H05000) and X-NICS of MEXT Grant No. JPJ011438. K.I. acknowledges a Grant-in-Aid for JSPS Fellow (Grant No. 22J22178) and GP-Spin at Tohoku University. S.I. acknowledges the Murata Science Foundation, the FRIS Creative Interdisciplinary Collaboration Program at Tohoku University, and JST, PRESTO Grant No. JPMJPR22B2. S.M. acknowledges CSRN in CSIS at Tohoku University.

APPENDIX A: MAGNETIC PROPERTY

The magnetic property was evaluated with vibrating-sample magnetometer measurements. Figure 6(a) illustrates the magnetic hysteresis loops for Bi(d_{Bi})/Co(5) samples with varying Bi thicknesses. The saturation magnetization M_s was evaluated from the magnetic hysteresis loops and is plotted as a function of Bi thickness in Fig. 6(b). The shape of the magnetic hysteresis loops and value of the saturation magnetization remained approximately constant with respect to Bi thickness. The average saturation magnetization was 1.2 MA/m.

APPENDIX B: ELECTRICAL CONDUCTIVITY OF THE SAMPLE

The electrical conductivities of thin-film samples were evaluated using the four-point probe method. Figure 7 plots the electrical sheet conductivity as a function of Bi thickness d_{Bi} . The slope of the sheet conductivity changes at approximately $d_{\text{Bi}} = 30$ nm. These data were used to calculate impedance Z [Eq. (3)]. The electrical conductivity at thicker regions was evaluated to be $1.9 \times 10^4 \Omega^{-1} \text{m}^{-1}$ based on the slope.

APPENDIX C: REFRACTIVE INDEX AND ABSORPTION OF LIGHT

Figure 8(a) shows the experimentally obtained reflectance (blue solid circles) and transmittance (red open squares) plotted as a function of Bi thickness d_{Bi} . The dashed curves denote R and T values calculated using the transfer matrix method [44] with the refractive indices listed in Table I for a glass substrate/Bi2(d_{Bi})/Co/MgO/Ta thin film (Bi single-

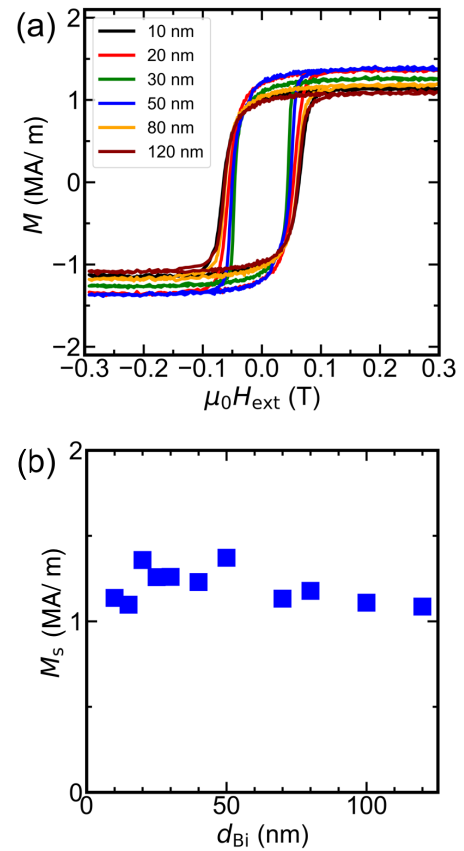


FIG. 6. (a) In-plane magnetic hysteresis loops of Bi(d_{Bi})/Co(5)/MgO(2)/Ta(2) (in nm) with various Bi thicknesses d_{Bi} . (b) The saturation magnetization obtained from the magnetic hysteresis loops plotted as a function of d_{Bi} .

layer model). The calculated results are consistent with those obtained experimentally in the thick region; however, there is a slight discrepancy in the thin region at $d_{\text{Bi}} < 30$ nm. A similar trend is observed for electrical conductivity: it varies at around $d_{\text{Bi}} = 30$ nm (see Appendix B). To explain the discrepancy in the thin region, the Bi layer was divided into interfacial (< 30 nm) and bulk layers (> 30 nm). The refractive index of

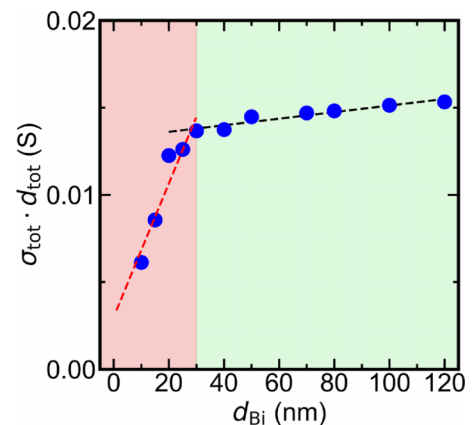


FIG. 7. Electrical sheet conductivities of thin films plotted as a function of d_{Bi} . The red and black dashed lines represent linear fitting in the thin region and thick region, respectively.

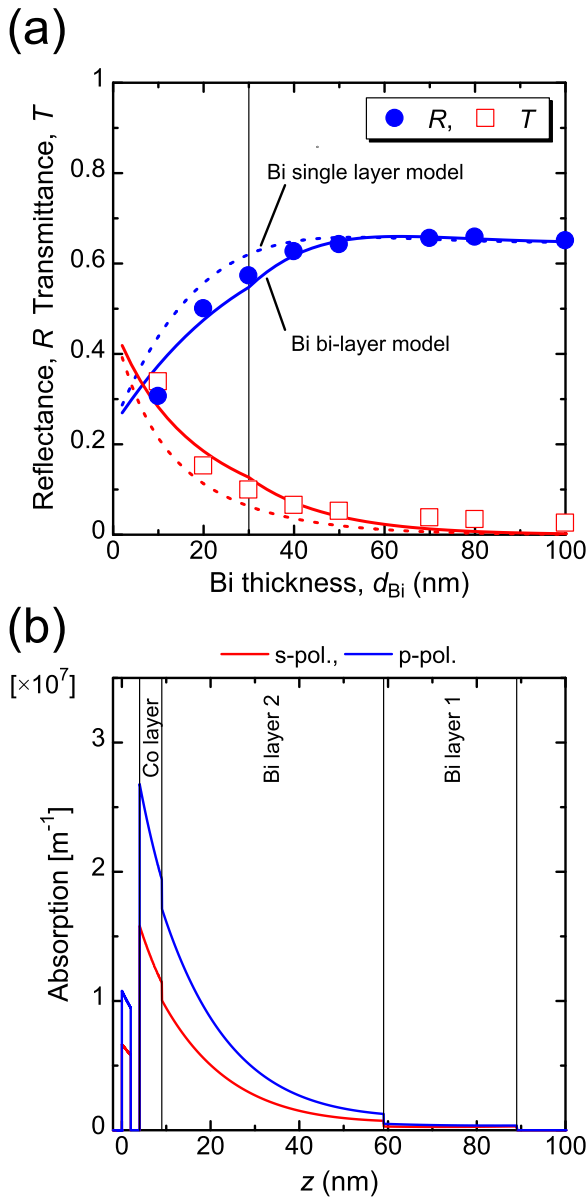


FIG. 8. (a) Bi thickness dependence of reflectance and transmittance. The dashed and solid curves denote calculated results using the transfer matrix method [44] for a Bi single-layer model and a Bi bilayer model, respectively. (b) Light absorption profile calculated using the Bi bilayer model for an 80-nm-thick Bi sample.

TABLE I. Refractive index (800 nm) used for the transfer matrix calculation. The real and imaginary parts of the refractive index at the interface Bi layer (Bi1) were obtained by fitting to experimental reflectance and transmittance data.

Material	Thickness (nm)	Refractive index
Ta	2	$1.11 + i3.48$ [51]
MgO	2	1.73 [52]
Co	5	$2.49 + i4.80$ [53]
Bi2	$\begin{cases} d_{\text{Bi}} - 30 \cdots d_{\text{Bi}} > 30 \\ 0 \cdots d_{\text{Bi}} \leq 30 \end{cases}$	$2.78 + i3.79$ [54]
Bi1	$\begin{cases} 30 \cdots d_{\text{Bi}} > 30 \\ d_{\text{Bi}} \cdots d_{\text{Bi}} \leq 30 \end{cases}$	$1.9 + i2.2$
Glass substrate	500 000	1.5

the bulk Bi layer (Bi2) was taken from the literature, while that of the interface Bi layer (Bi1) was obtained by fitting the experimental d_{Bi} dependence of R and T . The solid curves depicted in Fig. 8(a) correspond to R and T values calculated using the Bi bilayer model. R and T values at the thin region are explained well using the Bi bilayer model compared with the explanation provided by the Bi single-layer model. Figure 8(b) shows the calculated light absorption profile $a(z)$ for the Bi(80)/Co(5) sample. The light absorption of circularly polarized light corresponds to an average of light absorption with s and p polarizations, which is used to calculate the photon-spin injection [Eq. (6)].

APPENDIX D: ULTRAFAST DEMAGNETIZATION VIA TRMOKE MEASUREMENT

Laser-excited ultrafast demagnetization of Co was evaluated using the TRMOKE measurement. Figure 9(a) shows

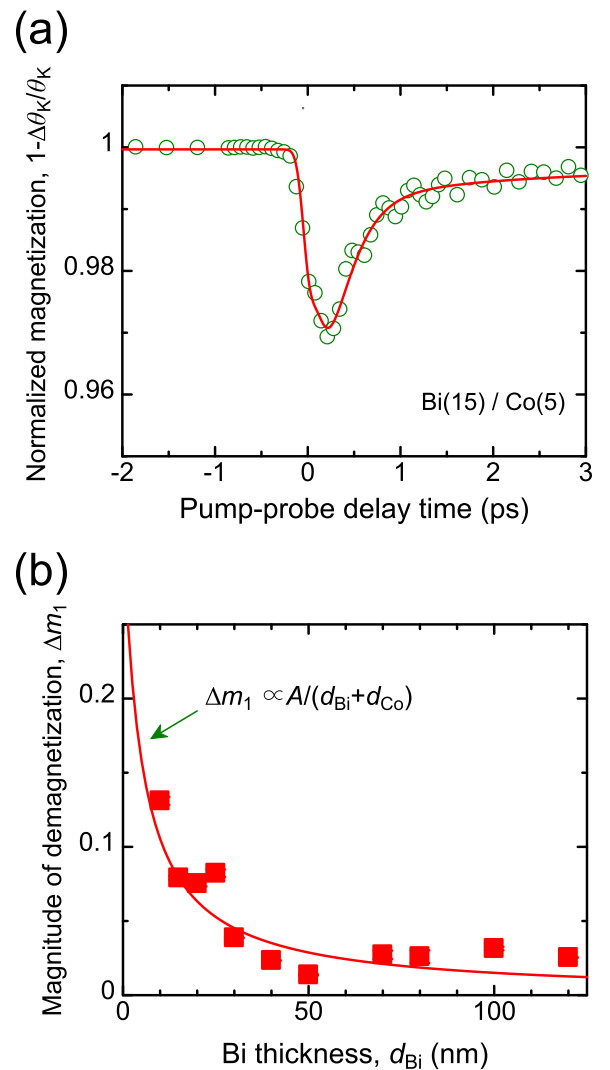


FIG. 9. (a) Demagnetization dynamics for a Bi(15)Co(5) bilayer film. The solid curve is the fitting result with Eq. (D1). (b) Magnitude of magnetization plotted as a function of Bi thickness. The solid curve represents a fitted result using a function inversely proportional to the total thickness of Co and Bi.

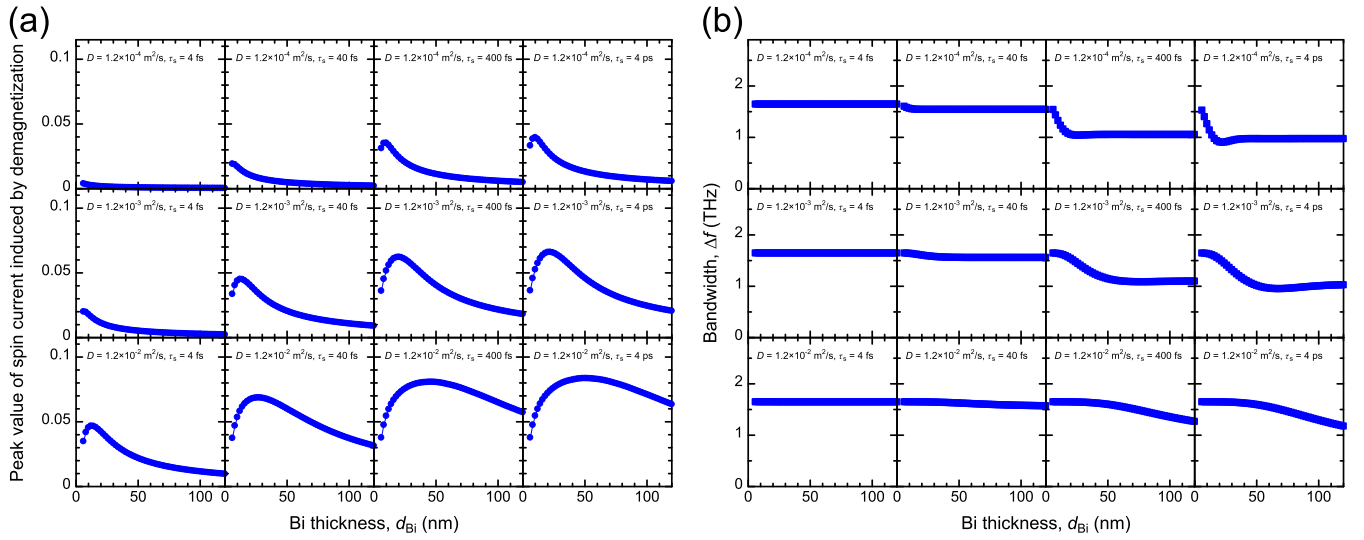


FIG. 10. Spin current (a) peak intensity and (b) bandwidth induced by laser induced demagnetization plotted as a function of Bi thickness d_{Bi} with different diffusion constants D and spin relaxation times τ_s .

normalized magnetization dynamics for the Bi(15)/Co(5) bi-layer film. The red solid curve denotes the fitting result obtained with the following equation [43,55]:

$$\frac{\Delta\theta_K(t)}{\theta_K} = \left[\left\{ \frac{\Delta m_1}{\sqrt{1+t/\tau_0}} - \frac{\Delta m_2 \tau_E - \Delta m_1 \tau_M}{\tau_E - \tau_M} e^{-t/\tau_M} - \frac{\tau_E(\Delta m_1 - \Delta m_2)}{\tau_E - \tau_M} e^{-t/\tau_E} \right\} \Theta(t) + \Delta m_3 \delta(t) \right] * G(t), \quad (\text{D1})$$

where Δm_1 , Δm_2 , and Δm_3 represent the change in the magnetization at the equilibrium state, maximum demagnetization, and state spin filling effect, respectively. τ_M and τ_E denote the demagnetization and remagnetization times, re-

spectively. $\Theta(t)$, $\delta(t)$, and $*$ are the Heaviside step function, Dirac delta function, and convolution product, respectively. The Bi thickness dependence of the demagnetization amplitude is well described with inverse total thickness, i.e., $\propto (d_{\text{Bi}} + d_{\text{Co}})^{-1}$, as shown in Fig. 9(b). The red solid curve denotes the fitting result.

APPENDIX E: SIMULATION WITH VARIOUS PARAMETERS

We performed a simulation with various diffusion constants D and spin relaxation times τ_s . D was assigned values of 1.2×10^{-4} , 1.2×10^{-3} , and 1.2×10^{-2} m²/s. τ_s was assigned values of 4 fs, 40 fs, 400 fs, and 4 ps. Figures 10(a) and 10(b) show the peak value and bandwidth of spin current induced by the demagnetization of the Co layer plotted as a function of Bi thickness d_{Bi} with different D and τ_s values.

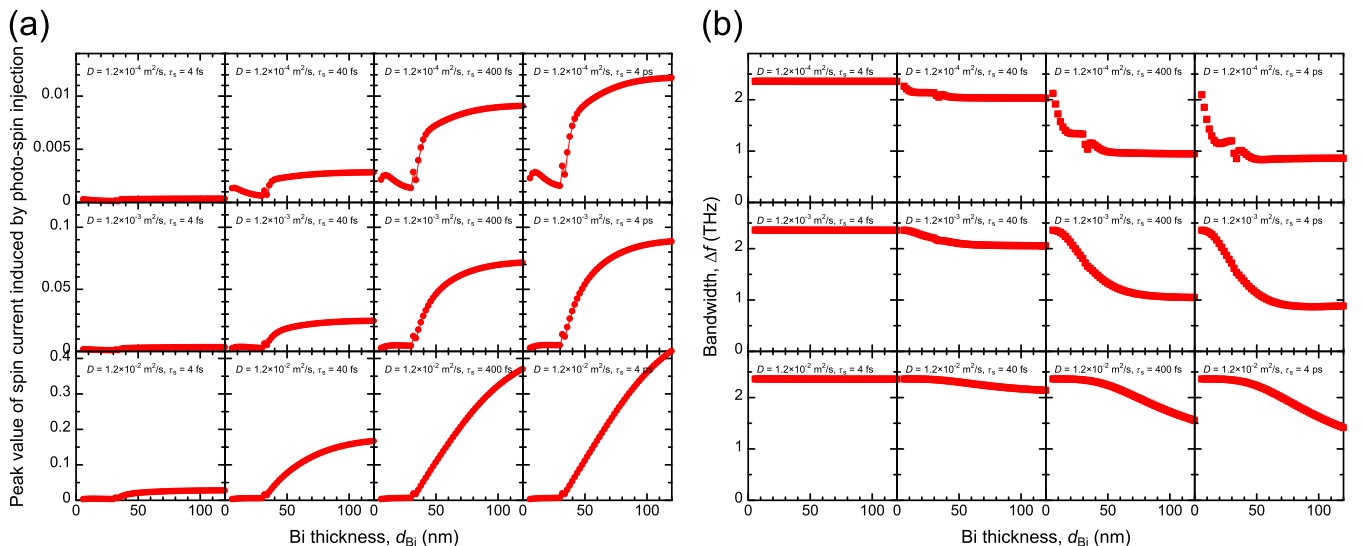


FIG. 11. Spin current (a) peak intensity and (b) bandwidth induced by photon-spin injection into Bi plotted as a function of Bi thickness d_{Bi} with different diffusion constants D and spin relaxation times τ_s .

Figures 11(a) and 11(b) show the peak value and bandwidth of spin current generated by photon-spin injection in the Bi layer plotted as a function of d_{Bi} with different D and τ_s values. D can be obtained by the Wiedemann-Franz law, given by $D = L\sigma/\gamma_e$, where L , σ , and γ_e are the Lorenz number,

electrical conductivity, and electronic heat capacity, respectively. When we use $\sigma = 1.9 \times 10^4$ ($\Omega \text{ m}$)⁻¹ evaluated by the four-point probe measurement and $\gamma_e = 0.37 \text{ J m}^{-3} \text{ K}^{-2}$ for Bi taken from the literature [56], $D = 1.2 \times 10^{-3} \text{ m}^2/\text{s}$ is obtained.

- [1] J. Sinova, S. O. Valenzuela, J. Wunderlich, C. H. Back, and T. Jungwirth, Spin Hall effect, *Rev. Mod. Phys.* **87**, 1213 (2015).
- [2] G. M. Choi, A. Schleife, and D. G. Cahill, Optical-helicity-driven magnetization dynamics in metallic ferromagnets, *Nat. Commun.* **8**, 15085 (2017).
- [3] K. Uchida, J. Xiao, H. Adachi, J. Ohe, S. Takahashi, J. Ieda, T. Ota, Y. Kajiwara, H. Umezawa, H. Kawai, G. E. W. Bauer, S. Maekawa, and E. Saitoh, Spin Seebeck insulator, *Nat. Mater.* **9**, 894 (2010).
- [4] T. Kawada, M. Kawaguchi, T. Funato, H. Kohno, and M. Hayashi, Acoustic spin Hall effect in strong spin-orbit metals, *Sci. Adv.* **7**, eabd9697 (2021).
- [5] K. Kondou, R. Yoshimi, A. Tsukazaki, Y. Fukuma, J. Matsuno, K. S. Takahashi, M. Kawasaki, Y. Tokura, and Y. Otani, Fermi level dependent charge-to-spin current conversion by Dirac surface state of topological insulators, *Nat. Phys.* **12**, 1027 (2016).
- [6] H. Wu, A. Chen, P. Zhang, H. He, J. Nance, C. Guo, J. Sasaki, T. Shirokura, P. N. Hai, B. Fang, S. A. Razavi, K. Wong, Y. Wen, Y. Ma, G. Yu, G. P. Carman, X. Han, X. Zhang, and K. L. Wang, Magnetic memory driven by topological insulators, *Nat. Commun.* **12**, 6251 (2021).
- [7] T. Tanaka, H. Kontani, M. Naito, T. Naito, D. S. Hirashima, K. Yamada, and J. Inoue, Intrinsic spin Hall effect and orbital Hall effect in $4d$ and $5d$ transition metals, *Phys. Rev. B* **77**, 165117 (2008).
- [8] K. Ando, S. Takahashi, K. Harii, K. Sasage, J. Ieda, S. Maekawa, and E. Saitoh, Electric Manipulation of Spin Relaxation Using the Spin Hall Effect, *Phys. Rev. Lett.* **101**, 036601 (2008).
- [9] C. F. Pai, L. Liu, Y. Li, H. W. Tseng, D. C. Ralph, and R. A. Buhrman, Spin transfer torque devices utilizing the giant spin Hall effect of tungsten, *Appl. Phys. Lett.* **101**, 122404 (2012).
- [10] L. Liu, C. F. Pai, Y. Li, H. W. Tseng, D. C. Ralph, and R. A. Buhrman, Spin-torque switching with the giant spin Hall effect of tantalum, *Science* **336**, 555 (2012).
- [11] D. Hou, Z. Qiu, K. Harii, Y. Kajiwara, K. Uchida, Y. Fujikawa, H. Nakayama, T. Yoshino, T. An, K. Ando, X. Jin, and E. Saitoh, Interface induced inverse spin Hall effect in bismuth/permalloy bilayer, *Appl. Phys. Lett.* **101**, 042403 (2012).
- [12] M. Matsushima, S. Miwa, S. Sakamoto, T. Shinjo, R. Ohshima, Y. Ando, Y. Fuseya, and M. Shiraishi, Sizable spin-transfer torque in the Bi/Ni₈₀Fe₂₀ bilayer film, *Appl. Phys. Lett.* **117**, 042407 (2020).
- [13] N. H. D. Khang, Y. Ueda, and P. N. Hai, A conductive topological insulator with large spin Hall effect for ultralow power spin-orbit torque switching, *Nat. Mater.* **17**, 808 (2018).
- [14] Q. D. Gibson, L. M. Schoop, L. Muechler, L. S. Xie, M. Hirschberger, N. P. Ong, R. Car, and R. J. Cava, Three-dimensional Dirac semimetals: Design principles and predictions of new materials, *Phys. Rev. B* **91**, 205128 (2015).
- [15] M. Dc, R. Grassi, J. Y. Chen, M. Jamali, D. Reifsnnyder Hickey, D. Zhang, Z. Zhao, H. Li, P. Quarterman, Y. Lv, M. Li, A. Manchon, K. A. Mkhoyan, T. Low, and J. P. Wang, Room-temperature high spin-orbit torque due to quantum confinement in sputtered Bi_xSe_(1-x) films, *Nat. Mater.* **17**, 800 (2018).
- [16] Y. Fuseya, M. Ogata, and H. Fukuyama, Transport properties and diamagnetism of Dirac electrons in bismuth, *J. Phys. Soc. Jpn.* **84**, 012001 (2015).
- [17] Y. Hirai, N. Yoshikawa, H. Hirose, M. Kawaguchi, M. Hayashi, and R. Shimano, Terahertz Emission from Bismuth Thin Films Induced by Excitation with Circularly Polarized Light, *Phys. Rev. Appl.* **14**, 064015 (2020).
- [18] H. Hirose, M. Kawaguchi, Y. C. Lau, Z. Chi, F. Freimuth, K. Takanashi, and M. Hayashi, Interface-enhanced helicity dependent photocurrent in metal/semimetal bilayers, *Phys. Rev. B* **103**, 174437 (2021).
- [19] K. Ando, M. Morikawa, T. Trypiniotis, Y. Fujikawa, C. H. W. Barnes, and E. Saitoh, Photoinduced inverse spin-Hall effect: Conversion of light-polarization information into electric voltage, *Appl. Phys. Lett.* **96**, 082502 (2010).
- [20] G. M. Choi, J. H. Oh, D. K. Lee, S. W. Lee, K. W. Kim, M. Lim, B. C. Min, K. J. Lee, and H. W. Lee, Optical spin-orbit torque in heavy metal-ferromagnet heterostructures, *Nat. Commun.* **11**, 1482 (2020).
- [21] S. Iihama, K. Ishibashi, and S. Mizukami, Interface-induced field-like optical spin torque in a ferromagnet/heavy metal heterostructure, *Nanophotonics* **10**, 1169 (2021).
- [22] S. Iihama, K. Ishibashi, and S. Mizukami, Photon spin angular momentum driven magnetization dynamics in ferromagnet/heavy metal bilayers, *J. Appl. Phys.* **131**, 023901 (2022).
- [23] M. Kawaguchi, H. Hirose, Z. Chi, Y. C. Lau, F. Freimuth, and M. Hayashi, Giant inverse Faraday effect in Dirac semimetals, [arXiv:2009.01388](https://arxiv.org/abs/2009.01388).
- [24] T. Kampfrath, M. Battiato, P. Maldonado, G. Eilers, J. Nötzold, S. Mährlein, V. Zbarsky, F. Freimuth, Y. Mokrousov, S. Blügel, M. Wolf, I. Radu, P. M. Oppeneer, and M. Münzenberg, Terahertz spin current pulses controlled by magnetic heterostructures, *Nat. Nanotechnol.* **8**, 256 (2013).
- [25] T. Seifert *et al.*, Efficient metallic spintronic emitters of ultra-broadband terahertz radiation, *Nat. Photonics* **10**, 483 (2016).
- [26] T. S. Seifert, N. M. Tran, O. Gueckstock, S. M. Rouzegar, L. Nadvornik, S. Jaiswal, G. Jakob, V. V. Temnov, M. Münzenberg, M. Wolf, M. Kläui, and T. Kampfrath, Terahertz spectroscopy for all-optical spintronic characterization of the spin-Hall-effect metals Pt, W and Cu₈₀Ir₂₀, *J. Phys. D* **51**, 364003 (2018).
- [27] G. M. Choi, B. C. Min, K. J. Lee, and D. G. Cahill, Spin current generated by thermally driven ultrafast demagnetization, *Nat. Commun.* **5**, 4334 (2014).
- [28] T. Lichtenberg, M. Beens, M. H. Jansen, B. Koopmans, and R. A. Duine, Probing optically induced spin currents using terahertz spin waves in noncollinear magnetic bilayers, *Phys. Rev. B* **105**, 144416 (2022).

- [29] R. Rouzegar, L. Brandt, L. Nádvořník, D. A. Reiss, A. L. Chekhov, O. Gueckstock, C. In, M. Wolf, T. S. Seifert, P. W. Brouwer, G. Woltersdorf, and T. Kampfrath, Laser-induced terahertz spin transport in magnetic nanostructures arises from the same force as ultrafast demagnetization, *Phys. Rev. B* **106**, 144427 (2022).
- [30] Y. Sasaki, K. Z. Suzuki, and S. Mizukami, Annealing effect on laser pulse-induced THz wave emission in Ta/CoFeB/MgO films, *Appl. Phys. Lett.* **111**, 102401 (2017).
- [31] Y. Sasaki, Y. Kota, S. Iihama, K. Z. Suzuki, A. Sakuma, and S. Mizukami, Effect of Co and Fe stoichiometry on terahertz emission from Ta/(Co_xFe_{1-x})₈₀B₂₀/MgO thin films, *Phys. Rev. B* **100**, 140406(R) (2019).
- [32] H. Idzuchi, S. Iihama, M. Shimura, A. Kumatani, S. Mizukami, and Y. P. Chen, Spin injection characteristics of Py/graphene/Pt by gigahertz and terahertz magnetization dynamics driven by femtosecond laser pulse, *AIP Adv.* **11**, 015321 (2021).
- [33] Y. Sasaki, G. Li, T. Moriyama, T. Ono, R. V. Mikhaylovskiy, A. V. Kimel, and S. Mizukami, Laser stimulated THz emission from Pt/CoO/FeCoB, *Appl. Phys. Lett.* **117**, 192403 (2020).
- [34] Y. Ogasawara, Y. Sasaki, S. Iihama, A. Kamimaki, K. Z. Suzuki, and S. Mizukami, Laser-induced terahertz emission from layered synthetic magnets, *Appl. Phys. Express* **13**, 063001 (2020).
- [35] G. Gallot and D. Grischkowsky, Electro-optic detection of terahertz radiation, *J. Opt. Soc. Am. B* **16**, 1204 (1999).
- [36] T. J. Huisman, R. V. Mikhaylovskiy, J. D. Costa, F. Freimuth, E. Paz, J. Ventura, P. P. Freitas, S. Blügel, Y. Mokrousov, Th. Rasing, A. V. Kimel, Femtosecond control of electric currents in metallic ferromagnetic heterostructures, *Nat. Nanotechnol.* **11**, 455 (2016).
- [37] D. Yue, W. Lin, J. Li, X. Jin, and C. L. Chien, Spin-to-Charge Conversion in Bi Films and Bi/Ag Bilayers, *Phys. Rev. Lett.* **121**, 037201 (2018).
- [38] S. Casalbuoni, H. Schlarb, B. Schmidt, P. Schmüser, B. Steffen, and A. Winter, Numerical studies on the electro-optic detection of femtosecond electron bunches, *Phys. Rev. Spec. Top. Accel. Beams* **11**, 072802 (2008).
- [39] Y. Sasaki, Y. Takahashi, and S. Kasai, Laser-induced terahertz emission in Co₂MnSi/Pt structure, *Appl. Phys. Express* **13**, 093003 (2020).
- [40] M. Battiato, K. Carva, and P. M. Oppeneer, Superdiffusive Spin Transport as a Mechanism of Ultrafast Demagnetization, *Phys. Rev. Lett.* **105**, 027203 (2010).
- [41] D. M. Nenno, B. Rethfeld, and H. C. Schneider, Particle-in-cell simulation of ultrafast hot-carrier transport in Fe/Au heterostructures, *Phys. Rev. B* **98**, 224416 (2018).
- [42] M. D. Stiles, J. Xiao, and A. Zangwill, Phenomenological theory of current-induced magnetization precession, *Phys. Rev. B* **69**, 054408 (2004).
- [43] S. Iihama, Y. Sasaki, H. Naganuma, M. Oogane, S. Mizukami, and Y. Ando, Ultrafast demagnetization of L1₀ FePt and FePd ordered alloys, *J. Phys. D* **49**, 035002 (2016).
- [44] J. Zak, E. R. Moog, C. Liu, and S. D. Bader, Universal approach to magneto-optics, *J. Magn. Magn. Mater.* **89**, 107 (1990).
- [45] B. Y. Mueller and B. Rethfeld, Relaxation dynamics in laser-excited metals under nonequilibrium conditions, *Phys. Rev. B* **87**, 035139 (2013).
- [46] M. Beens, R. A. Duine, and B. Koopmans, *s-d* model for local and nonlocal spin dynamics in laser-excited magnetic heterostructures, *Phys. Rev. B* **102**, 054442 (2020).
- [47] A. J. Schellekens, K. C. Kuiper, R. R. J. C. de Wit, and B. Koopmans, Ultrafast spin-transfer torque driven by femtosecond pulsed-laser excitation, *Nat. Commun.* **5**, 4333 (2014).
- [48] G. Li, R. V. Mikhaylovskiy, K. A. Grishunin, J. D. Costa, T. Rasing, and A. V. Kimel, Laser induced THz emission from femtosecond photocurrents in Co/ZnO/Pt and Co/Cu/Pt multilayers, *J. Phys. D* **51**, 134001 (2018).
- [49] J. Gorchon, S. Mangin, M. Hehn, and G. Malinowski, Is terahertz emission a good probe of the spin current attenuation length? *Appl. Phys. Lett.* **121**, 012402 (2022).
- [50] I. Timrov, T. Kampfrath, J. Faure, N. Vast, C. R. Ast, C. Frischkorn, M. Wolf, P. Gava, and L. Perfetti, Thermalization of photoexcited carriers in bismuth investigated by time-resolved terahertz spectroscopy and *ab initio* calculations, *Phys. Rev. B* **85**, 155139 (2012).
- [51] M. A. Ordal, R. J. Bell, R. W. Alexander, L. A. Newquist, and M. R. Querry, Optical properties of Al, Fe, Ti, Ta, W, and Mo at submillimeter wavelengths, *Appl. Opt.* **27**, 1203 (1988).
- [52] R. E. Stephens and I. H. Malitson, Index of refraction of magnesium oxide, *J. Res. Natl. Bur. Stand.* **49**, 249 (1952).
- [53] P. B. Johnson and R. W. Christy, Optical constants of transition metals: Ti, V, Cr, Mn, Fe, Co, Ni, and Pd, *Phys. Rev. B* **9**, 5056 (1974).
- [54] H. J. Hagemann, W. Gudat, and C. Kunz, Optical constants from the far infrared to the x-ray region: Mg, Al, Cu, Ag, Au, Bi, C, and Al₂O₃, *J. Opt. Soc. Am.* **65**, 742 (1975).
- [55] F. D. Longa, J. T. Kohlhepp, W. J. M. de Jonge, and B. Koopmans, Influence of photon angular momentum on ultrafast demagnetization in nickel, *Phys. Rev. B* **75**, 224431 (2007).
- [56] C. Kittel, *Introduction to Solid State Physics* (Wiley, New York, 2005).